Delft University of Technology

The roles of individual force components on the capture mechanism of bubbles around a vortical flow

Huang, Tzu Yao; Lidtke, Artur K.; Stigter, Rens; van Rijsbergen, Martijn X.; van Terwisga, Tom J.C.

DOI
10.1016/j.apor.2024.104154

Publication date
2024

Document Version
Final published version

Published in
Applied Ocean Research

Citation (APA)
Huang, T. Y., Lidtke, A. K., Stigter, R., van Rijsbergen, M. X., & van Terwisga, T. J. C. (2024). The roles of individual force components on the capture mechanism of bubbles around a vortical flow. *Applied Ocean Research*, *151*, Article 104154. https://doi.org/10.1016/j.apor.2024.104154

Important note
To cite this publication, please use the final published version (if applicable).
Please check the document version above.

Copyright
Other than for strictly personal use, it is not permitted to download, forward or distribute the text or part of it, without the consent of the author(s) and/or copyright holder(s), unless the work is under an open content license such as Creative Commons.

Takedown policy
Please contact us and provide details if you believe this document breaches copyrights.
We will remove access to the work immediately and investigate your claim.

This work is downloaded from Delft University of Technology.
For technical reasons the number of authors shown on this cover page is limited to a maximum of 10.

Applied Ocean Research 151 (2024) 104154

Contents lists available at ScienceDirect

Applied Ocean Research

journal homepage: www.elsevier.com/locate/apor

Invited paper

The roles of individual force components on the capture mechanism of bubbles around a vortical flow

Tzu-Yao Huang [a,*], Artur K. Lidtke [b], Rens Stigter [a], Martijn X. van Rijsbergen [b], Tom J.C. van Terwisga [a,b]

[a] *Faculty of Mechanical Engineering, Delft University of Technology, Mekelweg 2, Delft, 2628 CD, The Netherlands*
[b] *Maritime Research Institute Netherlands, Haagsteeg 2, Wageningen, 6708 PM, The Netherlands*

ARTICLE INFO

Keywords:
Lagrangian bubble tracking
Capture time analysis
Tip vortex cavitation inception

ABSTRACT

The mechanism of bubble capture in a vortical flow is investigated using a Lagrangian bubble tracking method. The motion of bubbles and the factors influencing their movement are examined. Detailed analysis is conducted on the roles played by each force component, such as the lift, added mass, and centrifugal forces, in the bubble capture process. An interesting finding is the identification of the stabilizing effect of the azimuthal lift force on the bubble capture mechanism. Furthermore, a model for capture time based on the radial force balance is also developed, and validated with existing experimental data. These findings, including the force mechanism and capture time model, provide a foundation for understanding the bubble capture process and can potentially inform future studies on tip vortex cavitation inception such as determining the cavitation hotspot.

1. Introduction

Fluid from the pressure side of a finite-span hydrofoil tip, for instance that of a propeller, is driven by the pressure gradient across the thickness of the foil and flows towards the suction side of the tip. This process leads to the formation of the so-called tip vortex. When the pressure in the vortex core drops to a sufficiently low level, the water there will begin to evaporate, triggering tip vortex cavitation. In ship design, there is a strong desire to avoid this phenomenon due to its potential for causing onboard vibration, erosion of blade tips and rudders, as well as generation of noise harmful to marine creatures (van Wijngaarden et al., 2005; van Terwisga et al., 2009; Bosschers, 2018; Erbe et al., 2019). Understanding the tip vortex cavitation inception dynamics would provide a deeper insight into how those unwanted impacts can be potentially avoided or mitigated. The bubble motion and dynamics around a vortex are crucial factors affecting tip cavitation inception (Arndt et al., 1991; Cheng et al., 2021). This study aims to investigate the background mechanism of how a bubble is captured by a vortical flow.

Roles of force components & capture time model. The forces exerted on the bubble, such as the lift, drag, and added mass, are the keys to the capture mechanism. Abdel-Maksoud et al. (2010), and Peters and el Moctar (2020) investigated bubble behaviors with different forces being neglected. They showed that the drag force was important to the overall motion as it made the bubble follow the flow and spirally migrate into the core. The researchers also observed that the pressure gradient force acted to draw the bubbles into the vortex core. Sridhar and Katz (1995) identified the force balance on a still bubble in solid body rotation flow and proposed a lift coefficient formulation accordingly. Finn et al. (2011) applied the same force balance scenario as (Sridhar and Katz, 1995) to devise a verification exercise. Zhang et al. (2016) proposed an ordinary differential equation model which could predict the trajectory of a bubble in a solid-body rotation vortex based on a simplified Lagrangian particle tracking method. This provides a simple framework for investigating the bubble motion around a vortex under different combinations of individual force components. Although researchers mentioned above have devoted themselves to force mechanism investigation, there are only few publications on the more detailed mechanism in the field of bubble behavior studies. Furthermore, most of the related studies are in the context of turbulence-bubble interaction (Mathai et al., 2020; Kelly et al., 2021; Mazzitelli et al., 2003) and not the tip vortex cavitation inception. It is important to expand the understanding of these forces in order to develop more robust models for the phenomenon of tip vortex cavitation. Interestingly but rationally, capture time (or entrapment time), which measures the time it takes for a bubble to be captured, is also highly influenced by the forces on the bubble. Oweis et al. (2005) developed a capture time model for bubbles around a stationary Lamb-Oseen vortex (also known as the Gaussian vortex) using the balance

---

* Corresponding author.
E-mail address: T.-Y.Huang@tudelft.nl (T. Huang).

https://doi.org/10.1016/j.apor.2024.104154
Received 8 March 2024; Received in revised form 26 July 2024; Accepted 31 July 2024
Available online 12 August 2024
0141-1187/© 2024 The Author(s). Published by Elsevier Ltd. This is an open access article under the CC BY license (http://creativecommons.org/licenses/by/4.0/).

between pressure gradient and drag forces in the radial direction. From the model, they found that the vortex Reynolds number, bubble radius, and the release position are key factors in bubble capture events. However, their analytical model deviated logarithmically from their numerical simulations. Consequently, the present work also aims to improve the robustness by further studying the roles of the individual force components.

Bubble tracking method. Modeling the motion of bubbles within a flow field has been a challenging task because cavitation research usually requires the resolution of small bubbles. To achieve accurate simulations while maintaining a reasonable computational effort, various approximate approaches have been developed. These numerical multiphase approaches can generally be divided into three categories: Eulerian mixture (Hirt and Nichols, 1981), Euler-Euler (Sokolichin et al., 1997; Afolabi and Lee, 2014), and Eulerian-Lagrangian methods (sometimes known as Lagrangian bubble tracking). The Eulerian-Lagrangian method is often preferred for researching the inception of tip vortex cavitation because it partially decouples the carrier fluid (liquid) and dispersed phase (bubbles), which allows for less stringent grid resolution requirements compared to the other two methods. Furthermore, important inception parameters such as nuclei effect and inception criteria can be considered and better integrated (Ji et al., 2024). Additionally, this approach enables the convenient monitoring of individual force components acting on a bubble, which is a key focus of the present work. Previous published research, such as Johnson and Hsieh (1966), Latorre (1982), Hsiao and Pauley (1999), and Wang et al. (2023), also made use of similar methods to study either tip vortex or sheet cavitation inception. Consequently, this multiphase modeling methodology has been adopted for the present study. This is coupled with the flow solution via a one-way coupling scheme that assumes small volume fractions of bubbles (Elghobashi, 1994). This coupling scheme has also been used and validated by other researchers (Hsiao et al., 2003; Ku et al., 2020) and the exact implementation utilized here was used to study sheet cavitation inception in van Rijsbergen and Lidtke (2020).

Tip vortex flow formulation. Real tip or trailing vortices are highly complex three-dimensional phenomena. Many researchers have dedicated themselves to developing mathematical formulations for the vortex, which are usually complex and may require a large number of parameters for closure (Moore et al., 1973; Uberoi et al., 1979; Phillips, 1981; Rule and Bliss, 1998; Anderson and Lawton, 2003). In order to allow more fundamental observations to be made and simple models to be developed, results presented here are based on the bubble behaviors around the stationary Lamb-Oseen vortex, which offers a simple but realistic environment.

2. Stationary Lamb-Oseen vortex

The stationary Lamb-Oseen vortex is a modification of the original Lamb-Oseen formulation that removes the time dependency. This allows the flow to be manipulated by choosing an arbitrary value for the viscous radius, r_v. The azimuthal flow velocity, U_θ, is given by:

$$U_\theta = \frac{\Gamma_\infty}{2\pi r}\left(1 - e^{-\varsigma r^2/r_\mathrm{v}^2}\right). \tag{1}$$

Here, r represents the radial distance from a field point to the vortex center, Γ_∞ indicates the total circulation of the field. $\varsigma \approx 1.2564$ is a constant chosen to make r_v be where the maximum velocity locates, which has the value of

$$U_\mathrm{v} = \lambda \frac{\Gamma_\infty}{2\pi r_\mathrm{v}}, \tag{2}$$

where $\lambda \approx 0.7153$. The radial profile of relevant variables are plotted in Fig. 1. The flow vorticity, pressure gradient, and pressure formulations are listed as they are the necessary input to solve bubble motion and dynamics (Bosschers, 2018):

$$\boldsymbol{\omega} = \varsigma \frac{\Gamma_\infty}{\pi r_\mathrm{v}^2} e^{-\varsigma r^2/r_\mathrm{v}^2}\hat{\mathbf{e}}_z, \tag{3}$$

$$\nabla P = -\rho \frac{\mathrm{D}\mathbf{U}}{\mathrm{D}t} = \rho \frac{U_\theta^2}{r}\hat{\mathbf{e}}_r, \tag{4}$$

$$\begin{aligned} P(r) = P_\infty - \frac{\rho \Gamma_\infty^2}{(2\pi r)^2}\Bigg\{ &\frac{1}{2} - e^{-\varsigma r^2/r_\mathrm{v}^2} + \frac{1}{2}e^{-2\varsigma r^2/r_\mathrm{v}^2} + \frac{\varsigma r^2}{r_\mathrm{v}^2}E_1\left(\frac{\varsigma r^2}{r_\mathrm{v}^2}\right) \\ &- \frac{\varsigma r^2}{r_\mathrm{v}^2}E_1\left(\frac{2\varsigma r^2}{r_\mathrm{v}^2}\right)\Bigg\}. \end{aligned} \tag{5}$$

Here, $E_1(z)$ is the exponential integral.

3. Lagrangian bubble tracking

3.1. Bubble motion equation

The one-way coupling Lagrangian bubble tracking involves tracking the motion of bubbles using the bubble motion equation, with the underlying flow field serving as an input. It is important to note that, one-way coupling scheme implies no momentum transferred from the bubbles to the flow.

The bubble motion equation describes the movement of a spherical bubble by accounting for different forces exerted on bubble from the carrier phase. In this research, only the added mass ($\mathbf{F}_\mathrm{A}$), pressure gradient ($\mathbf{F}_\mathrm{P}$), drag ($\mathbf{F}_\mathrm{D}$), lift ($\mathbf{F}_\mathrm{L}$) and Kelvin impulse forces ($\mathbf{F}_\mathrm{K}$) are considered. The gravity force and history force are negligible in the current scenario and including it would also significantly increase the complexity for the modeling (Morrison and Stewart, 1976; Hsiao and Pauley, 1999). The bubble motion equation used in the present work is

$$\left(m_\mathrm{B} + C_\mathrm{AM}\rho V_\mathrm{B}\right)\frac{\mathrm{d}\mathbf{U}_\mathrm{B}}{\mathrm{d}t} = \mathbf{F}_\mathrm{A} + \mathbf{F}_\mathrm{P} + \mathbf{F}_\mathrm{D} + \mathbf{F}_\mathrm{L} + \mathbf{F}_\mathrm{K}, \tag{6}$$

where m_B represents the net bubble mass, V_B the bubble volume, $\mathbf{U}_\mathrm{B}$ the bubble velocity vector, and ρ the carrier flow density. In this research, the added mass coefficient, C_AM, is set to $1/2$, as it is assumed that spherical bubbles dominate the entire period. In the equation,

$$\begin{aligned} \mathbf{F}_\mathrm{A} &= -C_\mathrm{AM}V_\mathrm{B}\nabla P, \\ \mathbf{F}_\mathrm{P} &= -V_\mathrm{B}\nabla P, \\ \mathbf{F}_\mathrm{D} &= C_D\frac{1}{2}\rho\pi R^2(\mathbf{U}-\mathbf{U}_\mathrm{B})|\mathbf{U}-\mathbf{U}_\mathrm{B}|, \\ \mathbf{F}_\mathrm{L} &= \frac{3}{8}C_L\rho V_\mathrm{B}\frac{(\mathbf{U}-\mathbf{U}_\mathrm{B})\times\boldsymbol{\omega}}{\alpha}, \\ \mathbf{F}_\mathrm{K} &= C_\mathrm{AM}\rho 4\pi R^2\dot{R}(\mathbf{U}-\mathbf{U}_\mathrm{B}). \end{aligned} \tag{7}$$

$\mathbf{U}$ denotes the carrier flow velocity, R the bubble radius, $\dot{R}$ the first derivatives of bubble radius, $\boldsymbol{\omega}$ the flow vorticity, and α in lift force represents the normalized shear rate, $|\boldsymbol{\omega}|R/|\mathbf{U}-\mathbf{U}_\mathrm{B}|$.

Solid particle drag formulation with no-slip boundary condition is applied to model spherical bubble drag. Marangoni effect introduces pre-stress condition as bubbles in the context of marine hydrodynamics are usually contaminated by non-uniform surfactant. In this study, a correction to the Stokes drag solution ($C_D = 24/\mathrm{Re}_\mathrm{B}$) proposed by Schiller and Neumann (1933) is applied without loss of generality:

$$C_D = \begin{cases} \frac{24}{\mathrm{Re}_\mathrm{B}}\left(1 + 0.15\,\mathrm{Re}_\mathrm{B}^{0.687}\right) & \text{if} \quad \mathrm{Re}_\mathrm{B} < 955, \\ 0.445 & \text{if} \quad \mathrm{Re}_\mathrm{B} \geq 955. \end{cases} \tag{8}$$

The bubble Reynolds number, Re_B, is defined by its radius and the relative velocity:

$$\mathrm{Re}_\mathrm{B} = \frac{2|\mathbf{U}-\mathbf{U}_\mathrm{B}|R}{\nu}, \tag{9}$$

where ν is the kinematic viscosity of the carrier fluid.

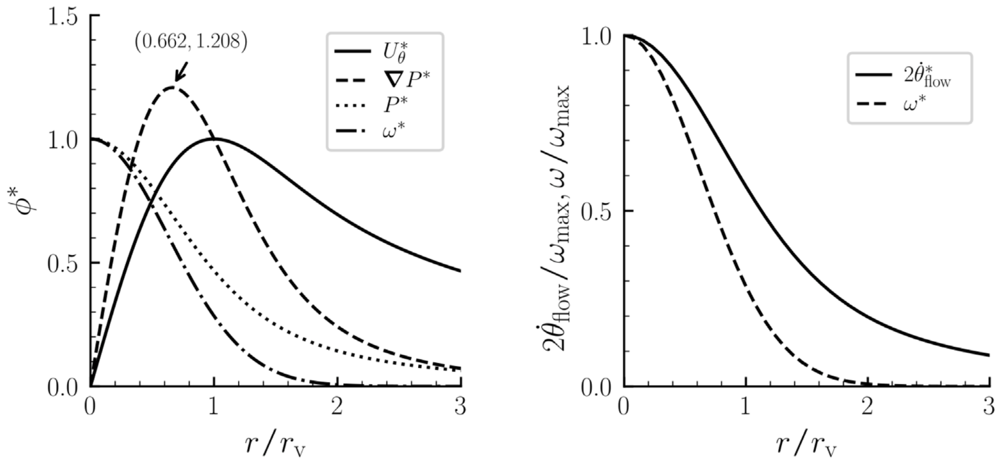

(a) Several important dimensionless variables.

(b) Angular velocity and the vorticity profiles.

Fig. 1. Some (normalized) physical quantity profiles of a stationary Lamb-Oseen vortex. $U_\theta^* = U_\theta/U_v$, $\nabla P^* = (U_\theta/U_v)^2/(r/r_v)$, $P^* = (P - P_\infty)/(P_{\min} - P_\infty)$, $\omega^* = \omega/\omega_{\max}$, $\dot{\theta}_{\mathrm{flow}} = U_\theta/r$.

The lift coefficient, C_L, for a bubble has several different formulations. Saffman (1965) derived the lift coefficient for very low $\mathrm{Re_B}$ and low shear flow, while Auton (1987) proposed a different formulation based on a mathematical derivation for high $\mathrm{Re_B}$ and low shear flow. Sridhar and Katz (1995) carried out a series of experiments and developed an empirical formula for the lift coefficient. Given the range of $\mathrm{Re_B}$ in the current research, this study will use Auton's formulation for the lift coefficient:

$$C_L = \frac{4}{3}\alpha. \tag{10}$$

α is the aforementioned normalized shear rate.

3.2. Bubble dynamics equation

The bubble dynamics equation describes the expansion and contraction of a single bubble. This research uses form proposed (Keller and Miksis, 1980) since it is proven to be the most accurate one in the first-order theory by Prosperetti and Lezzi (1986). It takes the form of

$$\left(1 - \frac{\dot{R}}{c}\right) R\ddot{R} + \frac{3}{2}\left(1 - \frac{\dot{R}}{3c}\right)\dot{R} = \frac{|\mathbf{U} - \mathbf{U}_\mathrm{B}|^2}{4} + \frac{1}{\rho}\left(1 + \frac{\dot{R}}{c}\right)(P_\mathrm{v} + P_\mathrm{g} - P) + \frac{1}{\rho}\frac{R}{c}\frac{\mathrm{d}P_\mathrm{g}}{\mathrm{d}t} - 4\nu\frac{\dot{R}}{R} - \frac{1}{\rho}\frac{2\eta}{R}, \tag{11}$$

where η represents surface tension at the bubble-water interface, and c is the sound speed in the host medium. The vapor pressure, P_v, could be conveniently chosen according to the assigned cavitation number. The gas pressure, P_g, is modeled via the polytropic process

$$P_\mathrm{g}(t) = P_\mathrm{g}(0)\left(\frac{R(0)}{R(t)}\right)^{3n}, \tag{12}$$

and n indicates the polytropic constant, which is $n = 1.4$ for the adiabatic condition. The external pressure acting on the bubble, P, is the interpolated flow pressure at the bubble center. Compared to the traditional formulation, in the present work one more term, highlighted in blue, is added in order to account for the slip velocity between the bubble and the host medium (Hsiao et al., 2000).

It is necessary to guarantee the bubble is initially released in an equilibrium state ($\ddot{R} = \dot{R} = 0$, $\mathbf{U} - \mathbf{U}_\mathrm{B} = \mathbf{0}$) for numerical stability:

$$P + \frac{2\eta}{R} - P_\mathrm{g} - P_\mathrm{v} = 0. \tag{13}$$

In practical terms, the equivalent bubble equilibrium radius (R_∞) is found at the reference condition ($P = P_\infty$) via Eq. (12): (Vallier, 2013)

$$\underbrace{\left(P_\infty + \frac{2\eta}{R_\infty} - P_\mathrm{v}\right) R_\infty^{3n}}_{\text{at the infinite reference condition.}} = \underbrace{\left(P_0 + \frac{2\eta}{R_0} - P_\mathrm{v}\right) R_0^{3n}}_{\text{at the initial release point.}}, \tag{14}$$

and the calculated results at the reference condition are further applied in the bubble dynamics computation, particularly Eq. (12). It should be noted that the absolute value of P_∞ is not important since the flow is incompressible. Furthermore, the $P_\infty - P_\mathrm{v}$ can be conveniently determined from the prescribed cavitation number.

3.3. Numerical solution approach

An in-house python code is developed to simulate the bubble behaviors. The bubble motion and dynamics equations are explicitly integrated in time until the bubbles reach their final radial position. The Cash–Karp method, an adaptive 4–5 Runge–Kutta approach, is adopted to control the relative error level to 10^{-5} in the simulations, as the nonlinearity of the bubble dynamic equation introduces a wide range of time scales. The relevant flow variables are computed at the bubble centers using the prescribed stationary Lamb-Oseen vortex.

4. Simulation setups and targets

A series of numerical simulation cases are performed in a stationary Lamb-Oseen vortex with $r_\mathrm{v} = 0.1\,\mathrm{m}$, which is similar to the previous studies such as Zhang et al. (2016), and Peters and el Moctar (2020). The circulation strength ranges from 0.29 to $29.0\,\mathrm{m^2/s}$, but the results from this study are mainly based on $\Gamma_\infty = 0.29\,\mathrm{m^2/s}$, which came from experiment of Oweis et al. (2005) and was further used in several numerical exercises such as Zhang et al. (2016), and Peters and el Moctar (2020). For each circulation case, a total of seventy bubbles are seeded in a matrix of seven different bubble sizes (R_0) and ten different release radial locations (r_0), each of which follows a geometric progression:

$$R_0/r_\mathrm{v} = 0.100, 0.064, 0.041, 0.027, 0.017, 0.011, 0.007;$$
$$r_0/r_\mathrm{v} = 0.316, 0.431, 0.586, 0.799, 1.088, 1.481, 2.017, 2.746, 3.740, 5.093.$$

Much smaller or further away bubbles are rare or insignificant in the context of the tip vortex cavitation inception, so they are not taken into account. Each bubble is released with a velocity identical to that of the flow at the release point.

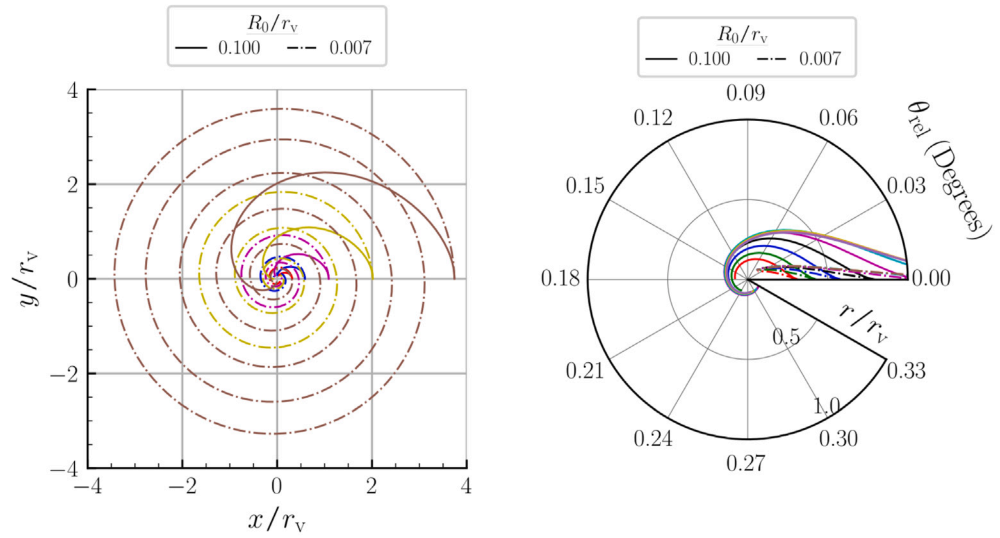

(a) Paths in the absolute frame of reference.

(b) Paths relative to the fluid carrier.

Fig. 2. Bubble paths for two different bubble sizes at various initial release positions. The colors indicate different release locations. The bubbles generally spiral towards the center with small deviations in azimuthal velocity relative to the background flow. Both the small (dashed-dotted line) and large (solid line) bubbles are presented.

The cavitation number is chosen to be the same as the one defined in Peters and el Moctar (2020), which is based on viscous core velocity and corresponding pressure:

$$\sigma_v = \frac{P_{vc} - P_v}{\frac{1}{2}\rho U_v^2} = 3.602,$$

which is fixed for each case with a different circulation strength to ensure a fair comparison. where P_{vc} is the pressure at the viscous core edge. This cavitation number corresponds to $\sigma = (P_\infty - P_v)/0.5\rho U_\infty^2 = 1.6$ if there is an background axial velocity (U_∞) of 5.6 m/s, which is similar to U_v/U_∞ value in experiment of Oweis et al. (2005). It is important to note that this study only investigates stationary Lamb-Oseen vortex which is still planar without an axial velocity.

To study the dynamics of the bubble population around the vortex core, the capture time will be carefully analyzed. The captured criterion is set to be a small radial coordinate value,

$$r_{cap}/r_v = 0.1,$$

which allows for some margin of error near the center but is also small enough to maintain the trend.

5. The roles of different forces

This section sheds light on the roles of the forces acting on a bubble and builds the foundation of the capture time model. First, preliminary observations are made based on the simulation results, and then a more detailed analysis upon the acceleration histories is conducted to reveal the roles of the forces.

5.1. Observations

There are two points that can help in discussing the roles of the force components. The first point is that polar mechanics is useful for describing the motion of bubbles in planar vortical flow. The paths with different conditions are sketched in Fig. 2(a). As can be seen, the paths are all spiral lines. Readers can refer to Appendix A for a brief introduction to the polar coordinate planar mechanics, which covers the essential inertial forces.

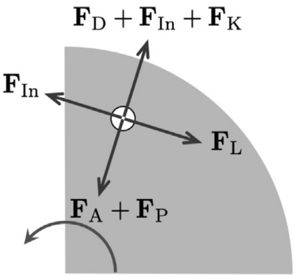

Fig. 3. The orientations of individual force components, which include added mass force due to the fluid acceleration ($\mathbf{F}_A$), pressure gradient force ($\mathbf{F}_P$), drag force ($\mathbf{F}_D$), Kelvin impulse force ($\mathbf{F}_K$), lift force ($\mathbf{F}_L$), and inertial force ($\mathbf{F}_{In}$). The detailed formulations of each force can be found in Eq. (7). The inertial forces include the radial centrifugal force and the azimuthal Coriolis force, which are introduced in Appendix A.

The other observation says the relative angular velocity is negligible, as inferred from the relative angular position in Fig. 2(b), where $\theta_{rel} = \int(\dot\theta - \dot\theta_{flow})\,dt$. Here, the former $\dot\theta$ represents the bubble angular velocity, and $\dot\theta_{flow}$ is the angular flow velocity. Note that the suffixes of the bubble kinematics in Newton's derivative notation are omitted henceforth for simplicity, such as $\dot r$, $\ddot\theta$, and $\dot x$. The relative angular coordinate, θ_{rel}, measures the accumulated deviation between the bubble and flow in the angular coordinate, and it reaches a maximum of only 0.33°. This indicates that the bubble mainly follows the azimuthal flow velocity throughout the traveling time. This confirms that the relative velocity, $\mathbf{U}_B - \mathbf{U}$, has major component in the radial direction, *i.e.*,

$$\mathbf{U}_B - \mathbf{U} \approx \dot r \hat{\mathbf{e}}_r + 0\hat{\mathbf{e}}_\theta. \tag{15}$$

Thus, only the radial component of the kinematics is important in the capture time analysis. A free-body diagram for the bubble can accordingly be depicted as Fig. 3. The lift acts in the azimuthal direction and the drag in the radial direction due to the relative velocity direction Note that this is contrary to cases involving settling points (Finn et al., 2011), since the bubble in capture process is still moving in azimuthal direction but that in the settling case stays at a fixed point.

5.2. Discussion

This section examines how different forces interact at different stages and what roles they play. The bubble accelerations, rather than the forces themselves, are analyzed to account for the mass difference

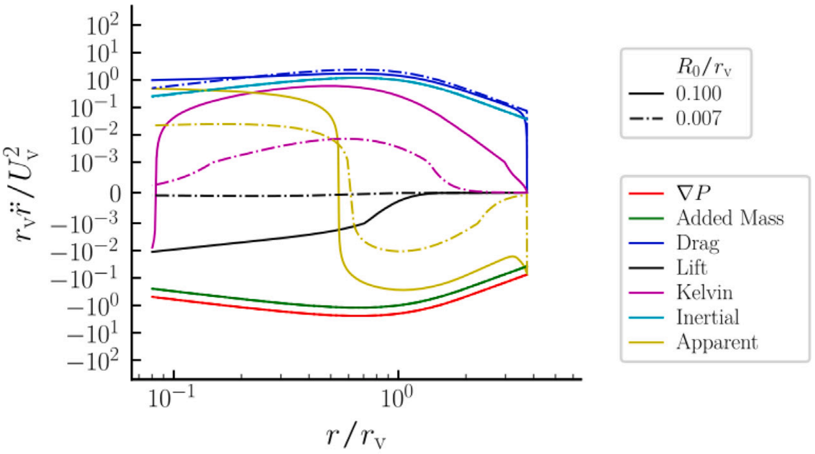

(a) Radial components.

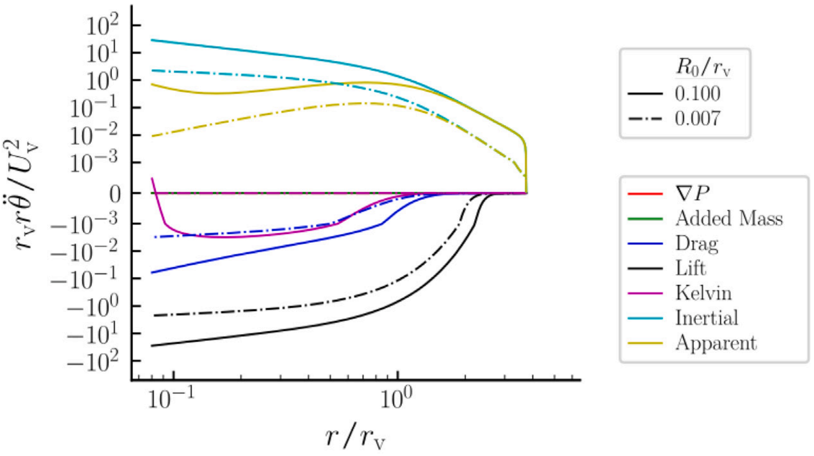

(b) Azimuthal components.

Fig. 4. The acceleration terms of bubbles released at $r_0/r_\mathrm{v} = 3.74$. Only the smallest (dashed-dotted lines) and the largest (solid lines) bubbles are presented for clarity. This is plotted using a symmetric logarithmic scale. When the ordinate value falls outside the thresholds of $\pm 10^{-3}$, the plot is shown in a logarithmic scale, whereas values within the thresholds are plotted using a linear scale.

between bubbles. Please refer to Appendix B for the simplified acceleration forms of the force components. It is important to note that those simplified forms are not utilized in either the simulation or the force calculation processes. Also, only the bubbles released relatively far from the vortex center are investigated, for they cover most of the motion stages. Furthermore, the accelerations are all normalized based on U_v and r_v, which could be regarded as the nominal centrifugal acceleration.

In the radial direction, the kinematics are influenced by four major components: added mass, pressure gradient, drag, and inertial (centrifugal) accelerations. The Kelvin impulse accelerations is relatively insignificant, as indicated by the lack of extreme bubble expansion, evident in Fig. 5. Generally, the (apparent) force balance is achieved during most of the traveling time because the magnitude of the apparent acceleration (see Appendix A for more details on the apparent acceleration/force) is negligible in comparison with the magnitude of dominating acceleration components such as drag and pressure gradient. Interestingly, the four aforementioned accelerations do not appear to be a function of bubble size, as indicated by the close matching between the dashed and solid lines in Fig. 4(a). This is because the added mass, pressure gradient, and inertial accelerations are purely proportional to U_θ^2/r or $r\dot\theta^2$, so the size of the bubble does not have an effect. Furthermore, the drag acceleration is linked to those three terms due to the apparent radial acceleration balance.

The azimuthal motion is primarily influenced by two components: the lift and inertial (Coriolis) accelerations. The drag and Kelvin impulse acceleration magnitudes are comparatively small due to the low relative azimuthal velocity. The lift plays a crucial role in balancing the inertial force, particularly within the viscous core. This is not a coincidence, but rather a result of the solid body rotation behavior in the core, as described by the relationship: $\omega = 2\dot\theta$; see Fig. 1(b). Using this relationship and the characteristics of the relative motion, it is possible to show that the inertial force is balanced with the lift (see Appendix B for the simplified lift acceleration formulation):

$$\begin{aligned} \text{Lift acceleration magnitude:} \quad & \left|(\mathbf{U}-\mathbf{U}_\mathrm{B})\times\boldsymbol{\omega}\right| = \omega|\dot r|,\\ \text{Coriolis acceleration magnitude:} \quad & \left|-2\dot r\dot\theta\hat{\mathbf{e}}_\theta\right| \qquad = \omega|\dot r|, \end{aligned} \tag{16}$$

where $\mathbf{U}-\mathbf{U}_\mathrm{B}$ is the relative velocity of which the radial component, $\dot r$, dominates, and ω currently represents the vorticity magnitude. Note that the bubble relative radial velocity ($\dot r$) is generally negative since the bubble is migrating inward.

In conclusion, the pressure gradient, added mass, drag, and centrifugal forces control the kinematics in the radial direction, while the lift and Coriolis forces govern the azimuthal direction, as predicted by the free body diagram shown in Fig. 3. All of the forces tend to maintain an apparent balance in each direction.

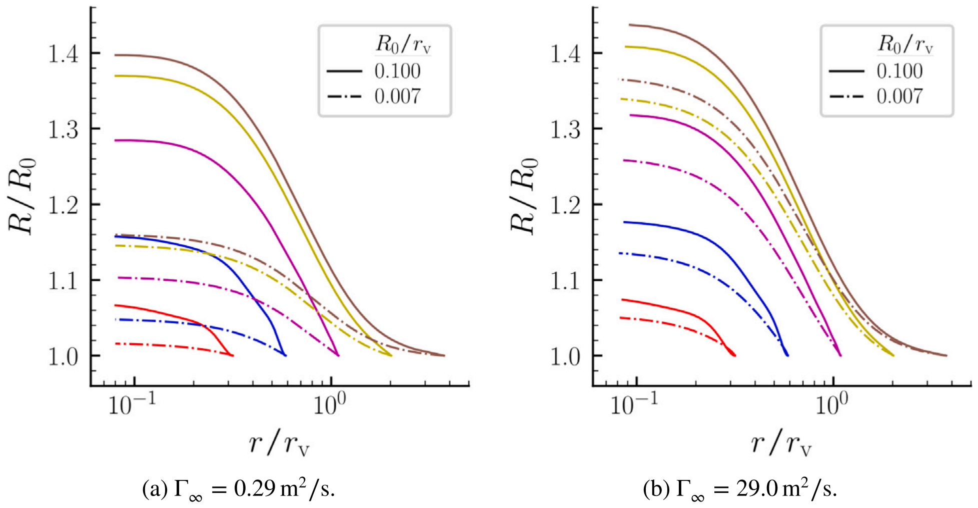

(a) $\Gamma_\infty = 0.29\,\mathrm{m}^2/\mathrm{s}$. (b) $\Gamma_\infty = 29.0\,\mathrm{m}^2/\mathrm{s}$.

Fig. 5. The growth of a bubble as it approaches the vortex center. Different colors represent different initial release positions, and both the small (dashed-dotted line) and large (solid line) bubbles are presented.

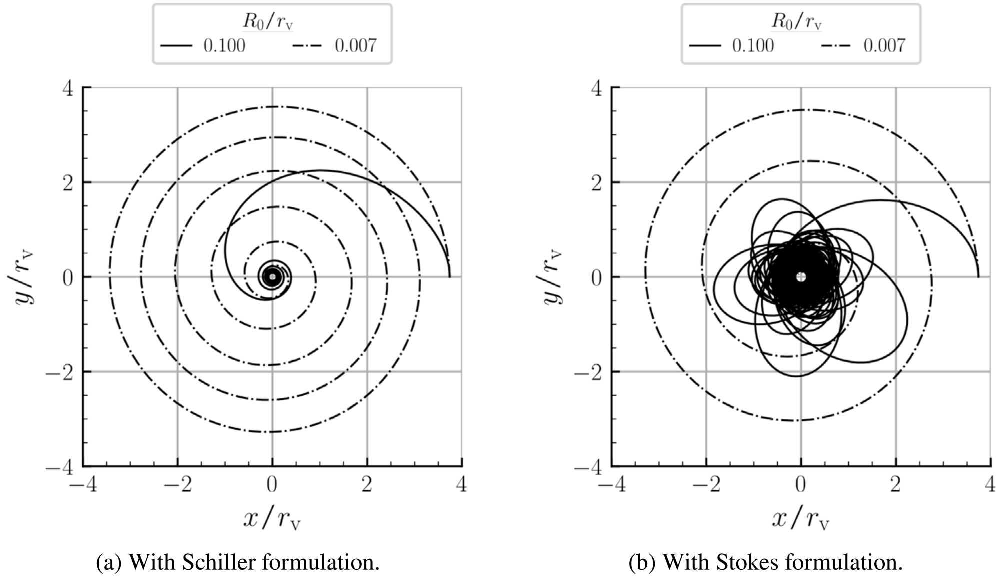

(a) With Schiller formulation. (b) With Stokes formulation.

Fig. 6. The bubble paths without the lift forces with two drag formulations. Both the small (dashed-dotted line) and large (solid line) bubbles are presented.

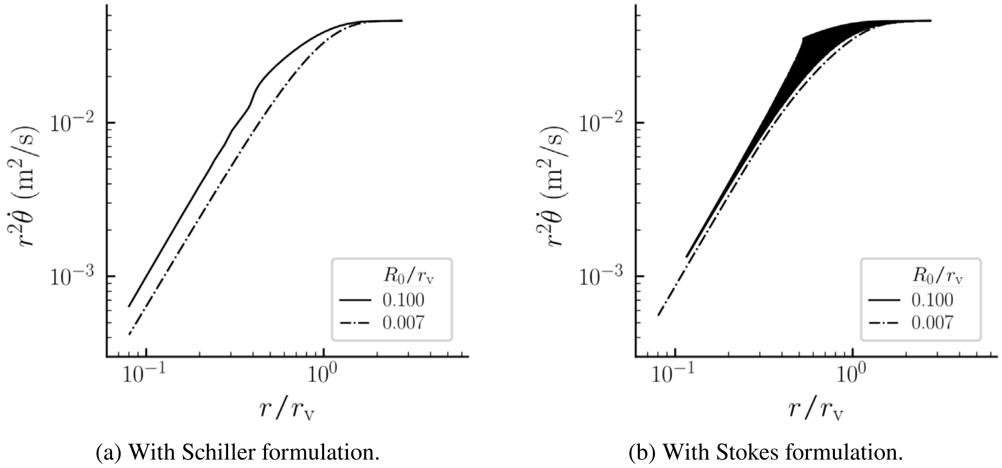

(a) With Schiller formulation. (b) With Stokes formulation.

Fig. 7. The angular momentum evolution of bubbles without the lift forces. The large bubble is characterized by solid lines and the small bubble by dashed-dotted lines.

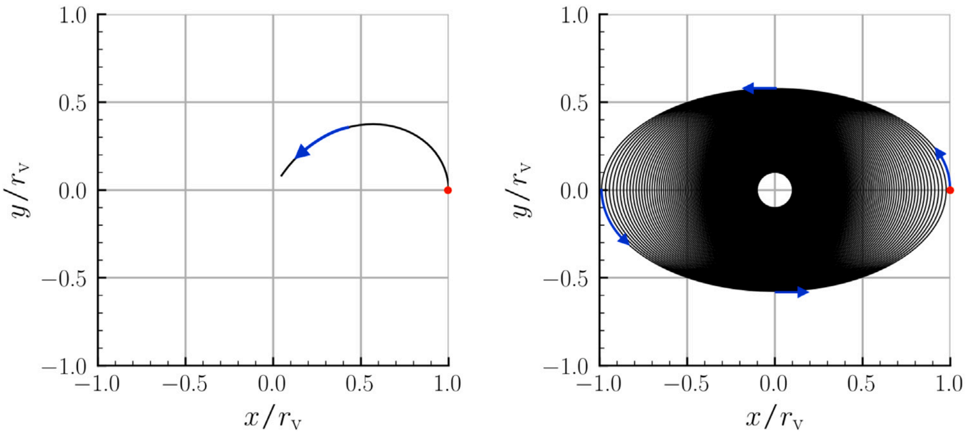

(a) Paths with the lift.

(b) Paths without the lift.

Fig. 8. Analytical path solutions from the two systems of ODEs (with or without lift) for a bubble released at the edge of a solid-body vortex. Only the large bubbles ($R_0/r_\mathrm{v} = 0.1$) are plotted. Red dotes indicate the starting points, and blue arrows are added to indicate the bubble's motion directions for clarity.

5.3. Remarks on the lift force effect

This section investigates the consequences of ignoring the lift force to show its importance, which is not often explicitly discussed in the literature. If the lift force is not included in the equation of motion, abiding by the conservation law of angular momentum, the azimuthal velocity of a bubble migrating into the core will increase. However, the resulting high level of centrifugal force will cause the bubble to be thrown into a greater radial distance again, similarly to the apsidal orbital precession in celestial mechanics. As a result, the motion near the center will be chaotic, particularly for the larger bubbles, which are not as effectively damped by drag as small bubbles, as shown in Fig. 6. The simulation uses the Stokes drag formulation illustrates the exaggerated effect of this phenomenon, as the drag force is much smaller in this model than in the Schiller model. The evolution of specific angular momentum ($r^2\dot{\theta}$), shown in Fig. 7, provides further insight into this phenomenon. The angular momentum of the large bubble tends to stay at the same level rather than directly decrease, indicating that there is not enough azimuthal force-induced moment to reduce the angular momentum in the absence of the lift force. In contrast, small bubbles tend to exhibit an ordered trend, as the drag force is still relatively large and can play a role similar to the lift force in balancing the Coriolis force.

Next, a linearized ordinary differential equation (ODE) model, inspired by Zhang et al. (2016), is introduced to further examine the bubble behavior. The vortex is simplified into the solid-body rotation with identical circulation, with the vorticity evenly distributed within the viscous radius. In this case, the bubble motion equation including the lift force can be simplified into a system of two-dimensional ODEs:

$$\begin{aligned} &\frac{\mathrm{d}^2x}{\mathrm{d}t^2} + a\frac{\mathrm{d}x}{\mathrm{d}t} + \omega\frac{\mathrm{d}y}{\mathrm{d}t} + \frac{1}{4}\omega^2 x = -\frac{1}{2}a\omega y, \\ &\frac{\mathrm{d}^2y}{\mathrm{d}t^2} + a\frac{\mathrm{d}y}{\mathrm{d}t} - \omega\frac{\mathrm{d}x}{\mathrm{d}t} + \frac{1}{4}\omega^2 y = \frac{1}{2}a\omega x, \end{aligned} \tag{17}$$

where

$$a = \frac{9\nu}{R^2}, \quad \text{and} \quad \omega = \frac{\Gamma_\infty}{\pi r_\mathrm{v}^2}.$$

These equations have already simplified the drag force using the Stokes formulation. The terms at right hand side sequentially represent (1) inertial force, (2) bubble velocity in drag force, (3) bubble velocity in lift force, (4) pressure gradient force and carrier velocity in lift force. The right hand side takes carrier velocity in drag force into account. As shown in Eq. (17), even if the bubbles are large, the shaded term, related to the lift, can still provide damping and eventually stabilize the system. Without the lift force, the equations of motion are:

$$\begin{aligned} &\frac{\mathrm{d}^2x}{\mathrm{d}t^2} + a\frac{\mathrm{d}x}{\mathrm{d}t} + \frac{3}{4}\omega^2 x = -\frac{1}{2}a\omega y, \\ &\frac{\mathrm{d}^2y}{\mathrm{d}t^2} + a\frac{\mathrm{d}y}{\mathrm{d}t} + \frac{3}{4}\omega^2 y = \frac{1}{2}a\omega x. \end{aligned} \tag{18}$$

Thus, in the absence of the lift-induced damping terms, the system becomes underdamped for large enough bubbles. This can be seen in the comparison of analytical path solutions in Fig. 8, where the solution with the lift exhibits overdamped behavior while the solution without the lift exhibits underdamped behavior. It may be worth noting that the study by Zhang et al. (2016) did not take the lift force into account in their analysis correctly. The proper equation with lift to use in this case would be Eq. (17) rather than Eq. (18). It should also be noted that the coefficients of the last terms at left hand side are different from Eq. (17) since the lift force is measured with relative velocity, including influence of the carrier velocity.

In summary, the lift force acts in the azimuthal direction and decreases the angular momentum. By balancing out the Coriolis force, it helps to stabilize the system.

5.4. Remarks on applying different force formulations

In essence, the bubble strives to achieve a balance of forces in both the azimuthal and radial directions. When different formulations are applied, as long as the variations in force are not orders of magnitude apart, the overall mechanism remains consistent. The inclusion of the history force aids in balancing the added mass force in the radial direction; however, its impact is minimal due to its generally small magnitude. Variations in drag formulations primarily affect the magnitude of the radial velocity. Even if different lift force formulations, if not drastically different, alter the force balance in the azimuthal direction, the drag force will adjust to compensate, thereby maintaining similar kinematic.

6. Capture time model

This section addresses the capture time model with its assumptions, development, verification, and limitations. This model is inspired by Oweis et al. (2005) but a more in-depth analysis is presented based on the previous analysis of the forces' roles, especially the apparent radial force balance.

Table 1
Variations of the capture time model regarding the azimuthal velocity formulations and the drag formulation.

C_D	U_θ	
	Ideal vortex	Lamb-Oseen vortex
Stokes	✓	✓
Schiller	✗	✓

6.1. Assumptions

The capture time model is based on the radial mechanics as the bubble azimuthal velocity aligns with the flow velocity. This allows for the calculation of bubble radial velocity from the azimuthal velocity along with the apparent force balance explored before. The Kelvin impulse is ignored during developing the model as the bubble expansion is not significant enough during the capturing stage.

In a nutshell, the polar coordinate mechanics is applied to assist the analysis, and three other assumptions based on the observations are introduced to construct the model:

$$\dot{\theta} - \dot{\theta}_{\text{flow}} = 0, \quad \dot{R} = 0, \quad \ddot{r} = 0.$$

6.2. Development of the capture time model

The capture time model will be derived using the three assumptions mentioned above. The idea is that the apparent radial force balance can be used to predict the bubble radial velocity based on the azimuthal flow velocity, and the bubble's capture time can be calculated from the time integral of the reciprocal of the bubble radial velocity.

As already shown in Fig. 3, the apparent radial force balance reads

$$F_{\text{A}} + F_{\text{P}} + F_{\text{D}} + F_{\text{In}} = 0, \tag{19}$$

where F_{In} represents the centrifugal force as an inertial force stemming from the polar coordinate reference frame. Given that the added mass dominates the total apparent mass, the force balance could be easily transformed into the following acceleration balance based on Eq. (30):

$$\underbrace{-\frac{U_\theta^2}{r}}_{\text{Added mass}} \quad \underbrace{-2\frac{U_\theta^2}{r}}_{\text{Pressure gradient}} \quad \underbrace{-\frac{3C_D}{4R}|\dot{r}|\dot{r}}_{\text{Drag}} \quad + \quad \underbrace{r\dot{\theta}^2}_{\text{Centrifugal}} \quad = 0, \tag{20}$$

where the azimuthal flow velocity U_θ has been shown to be mostly identical to the bubble azimuthal velocity $r\dot{\theta}$. The added mass and centrifugal components can cancel out each other:

$$2\frac{U_\theta^2}{r} = -\frac{3C_D}{4R}|\dot{r}|\dot{r}. \tag{21}$$

The bubble radial velocity can then be deduced from the azimuthal flow velocity and the radial position of the bubble. The result is similar to Oweis et al. (2005), but the roles of added mass and centrifugal forces in Eq. (19) are highlighted.

To test the limits of the proposed simplifications, two formulations for both the azimuthal velocity (ideal and Lamb-Oseen) and the drag coefficient (Stokes and Schiller) are applied. This results in four possible representations of the radial velocity, but the combination of the ideal vortex and Schiller drag is not considered since the other three already provide sufficient insights into the modeling simplifications. These variations are summarized in Table 1.

Models using the Stokes drag formulation can be expressed analytically, but the model using the Schiller drag cannot. As an example, the derivation process for the combination of the Lamb-Oseen vortex and Stokes drag will be shown. From the apparent radial acceleration balance, the corresponding inward radial velocity is

$$\dot{r} = -\frac{2R^2}{9\nu}\frac{U_\theta^2}{r} \quad \text{with} \quad U_\theta = \frac{\Gamma_\infty}{2\pi r}\left(1 - e^{-\varsigma r^2/r_{\text{v}}^2}\right). \tag{22}$$

The capture time, with some tedious integration, is thus

$$t_{\text{c}} = \int_{r_0}^{r_{\text{cap}}} \frac{1}{\dot{r}}\,\mathrm{d}r = \frac{9\nu\pi^2 r_{\text{v}}^4}{\Gamma_\infty^2 R^2}\left(\frac{r^{*4}}{2} + \frac{\log\left(1 - e^{-\varsigma r^{*2}}\right)}{\varsigma^2} - \frac{r^{*2}e^{-\varsigma r^{*2}}}{\varsigma(1 - e^{-\varsigma r^{*2}})} + \frac{\mathrm{Li}_2(e^{-\varsigma r^{*2}})}{\varsigma^2}\right)\Bigg|_{r^*_{\text{cap}}}^{r^*_0}, \tag{23}$$

where r^* is the normalized radial coordinate by the viscous radius, r_{cap} is the prescribed capture radius, and Li_2 is known as Spence's function or the dilogarithm.

The Buckingham Π theorem indicates that five carefully-chosen dimensionless parameters could describe the system as well:

$$t^*_{\text{c}} = \frac{t_{\text{c}}U_{\text{v}}}{r_{\text{v}}},\ R^*_0 = \frac{R_0}{r_{\text{v}}},\ r^*_0 = \frac{r_0}{r_{\text{v}}},\ r^*_{\text{cap}} = \frac{r_{\text{cap}}}{r_{\text{v}}},\ \text{and } \mathrm{Re}_{\text{v}} = \frac{U_{\text{v}}r_{\text{v}}}{\nu}.$$

Here, the capture time is normalized by the revolution time scale of the vortex, and the circulation is embedded into the Reynolds number characterized by the vortex diffusion scale. Thus, the capture time could be rewritten in a dimensionless way:

$$t^*_{\text{c}} = \frac{9}{4}\frac{\lambda^2}{\mathrm{Re}_{\text{v}}R^{*2}_0}\left(\frac{r^{*4}}{2} + \frac{\log\left(1 - e^{-\varsigma r^{*2}}\right)}{\varsigma^2} - \frac{r^{*2}e^{-\varsigma r^{*2}}}{\varsigma(1 - e^{-\varsigma r^{*2}})} + \frac{\mathrm{Li}_2(e^{-\varsigma r^{*2}})}{\varsigma^2}\right)\Bigg|_{r^*_{\text{cap}}}^{r^*_0}. \tag{24}$$

In the original work of Oweis et al. (2005), the flow velocity was simplified using an ideal vortex field with the same circulation strength. Therefore, their capture time model was formulated similarly, but without the highlighted terms in Eq. (24).

However, using the Stokes drag formulation limits the analysis of large bubbles, for which the real drag coefficient reaches a plateau of 0.445 when Re_{B} is sufficiently large, as shown in the Schiller sphere drag formulation:

$$C_D = \begin{cases} \frac{24}{\mathrm{Re}_{\text{B}}}\left(1 + 0.15\,\mathrm{Re}_{\text{B}}^{0.687}\right) & \text{if} \quad \mathrm{Re}_{\text{B}} < 955, \\ 0.445 & \text{if} \quad \mathrm{Re}_{\text{B}} \geq 955. \end{cases} \tag{8 revisited}$$

Thus the combination of the Schiller drag formulation and the Lamb-Oseen vortex is of the most interest. The Schiller drag formulation is complex, but the radial velocity could still be easily determined by using numerical root finding and numerical integration methods.

In this subsection, three variations of the capture time model have been introduced, all of which are based on the apparent radial acceleration balance in polar coordinates.

6.3. Comparison between model variations

This section discusses how the choices of vortex and drag formulations affect capture time results.

As shown in Fig. 9, model variations using the Stokes formulation significantly underestimate capture time because the Stokes drag coefficient is relatively low in the high Re_{B} region, resulting in a sizeable inward radial velocity due to the pressure gradient (Eq. (21)). On the other hand, including the Lamb-Oseen vortex in the model improves accuracy because the pressure gradient of an ideal vortex differs significantly from that of a Lamb-Oseen vortex, especially within the viscous core.

In summary, simplification of the model using either an ideal vortex or the Stokes drag can significantly underestimate the capture time. Therefore, only the combination of the Lamb-Oseen vortex and the Schiller formulation, which was also used in the numerical simulation, will be considered in the following discussions and detailed examinations.

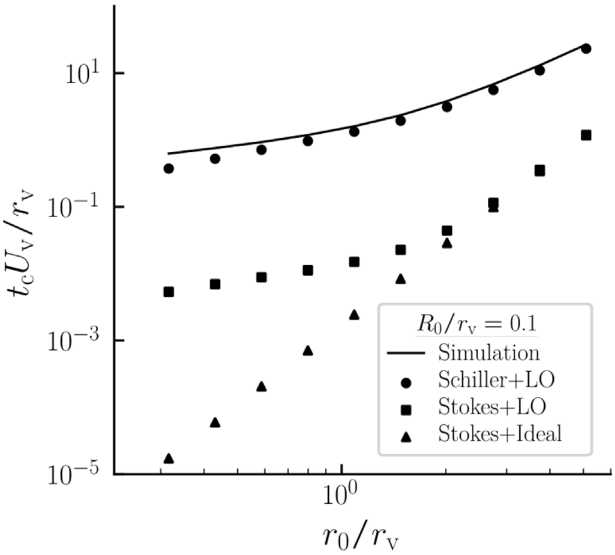

Fig. 9. Comparison between capture time ($t_{\rm c}$) model variations. The abscissa represents the normalized initial release position ($r_0/r_{\rm v}$), and the bubbles with the radius of $0.1r_{\rm v}$ are chosen to clearly demonstrate the comparison. As mentioned in Table 1, three model variations are presented to be compared with the numerical simulation: Schiller drag formulation with stationary Lamb-Oseen flow field ("Schiller+LO"), Stokes drag formulation with stationary Lamb-Oseen flow field ("Stokes+LO"), and Stokes drag formulation with ideal vortex flow field ("Stokes+Ideal").

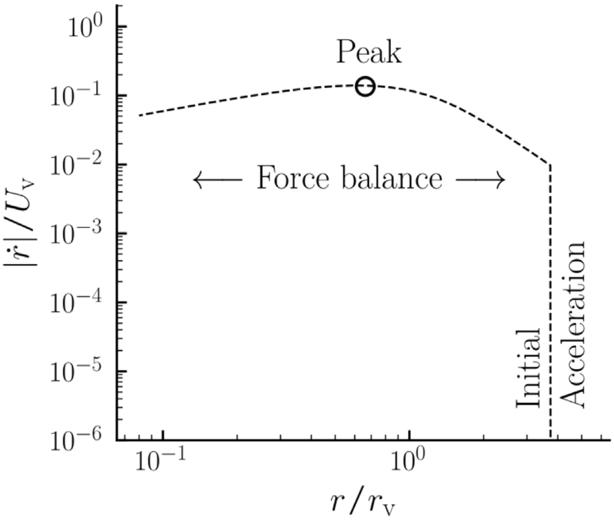

Fig. 10. Schematics of the bubble radial velocity profile regarding the radial position. The bubble is of $R_0 = 0.007r_{\rm v}$ and $r_0 = 3.74r_{\rm v}$. Two stages are present: the initial acceleration and the force balance stage. The initial acceleration stage is characterized by the straight vertical line, while the force balance phase is represented by the rest curve resembling a small hill.

6.4. Radial velocity prediction

The capture time model aims to estimate the bubble radial velocity based on the prescribed flow azimuthal velocity. Therefore, it is crucial to have accurate bubble velocity profiles, particularly in terms of radial position.

According to Fig. 10, a representative extraction of Fig. 11, the bubble typically goes through two stages in the current simulation, the initial acceleration stage and the force balance stage:

- Initial acceleration stage (the vertical straight lines):
  The bubble is not initially released with forces balanced in radial direction when performing the numerical simulation. Thus, the bubble will continue to accelerate until the relative radial velocity becomes high enough for the drag force to be comparable to the inward force in the simulation. Note that the stage results from the absence of proper initial kinematic conditions, which requires further attention in future studies.
- Force balance stage (the hill-like curve):
  During the force balance stage, the added mass, pressure gradient, centrifugal, and drag forces cancel each other out, resulting in a state of force equilibrium. This can be seen from the magnitude of the apparent acceleration represented by the mustard yellow line in Fig. 4(a). The bubble reaches this equilibrium from the previous stage and remains in this state for the remainder of the duration, as the pressure gradient changes within the bubble's response time.
  Notably, the bubble reaches its maximum velocity at roughly $r/r_{\rm v} = 0.66$ as the pressure gradient and added mass forces reach their maximum, previously shown in Fig. 1(a). This explains why the peaks occur at similar magnitude and spatial location for identical bubbles even with different released point, as demonstrated in Fig. 11.

If the model can more accurately capture the bubble velocity evolution in the scenario, it will be better able to assess the capture time. It is expected that the capture time of small bubbles will be predicted more accurately than that of large bubbles, due to the longer time scale and sharper transition between two stages for small bubbles. The following section will examine the numerical simulation and confirm the importance of the predicted velocity profile presented here.

6.5. The capture time trend and the model limitations

Figs. 12 and 13 show the capture time comparisons regarding the initial release position and bubble radius, respectively. Intuitively, a bubble released closer to the vortex center will be captured more quickly. In general, larger bubbles are also captured more rapidly than smaller ones, due to the dominant influence of the pressure gradient term in Eq. (30) over the drag term as the bubble radius increases.

Fig. 14 shows the effect of the remaining influencing parameter, the core Reynolds number (which is effectively the circulation strength). It can be seen that stronger circulation leads to faster bubble capture. The plateau of the *dimensionless* capture time is due to the plateau in the drag coefficient at high $\mathrm{Re_B}$, where the inward radial velocity is proportional to the azimuthal velocity and therefore proportional to the circulation strength to the power of one (see Eq. (21)). This can be more clearly seen in Fig. 11, where the normalized inward radial velocities do not change with the circulation strength for large bubbles, leading to nearly identical *dimensionless* capture times for different core Reynolds numbers.

The capture time model based on the Schiller drag can accurately predict the capture time in most cases. This supports the assumption of force balance in general. Additional evidence can be found in Fig. 11, where the velocity profiles predicted by the model match the simulation results well. However, there is a larger deviation for large bubble cases due to the acceleration effect, which is sometimes unavoidable when the time scale is short and the initial acceleration stage occupies a significant portion of the total simulation time. In contrast, the small bubble cases have a sharper transition from the initial acceleration stage to the force balance stage, leading to better predictions of the capture time.

The model has been validated against experimental results. Oweis et al. (2005) measured the capture time of laser-induced bubbles entrapped by a line vortex. The dimensionless capture time predicted by the current model is based on the balanced velocity from the Lamb-Oseen vortex and Schiller drag. The comparison between the model

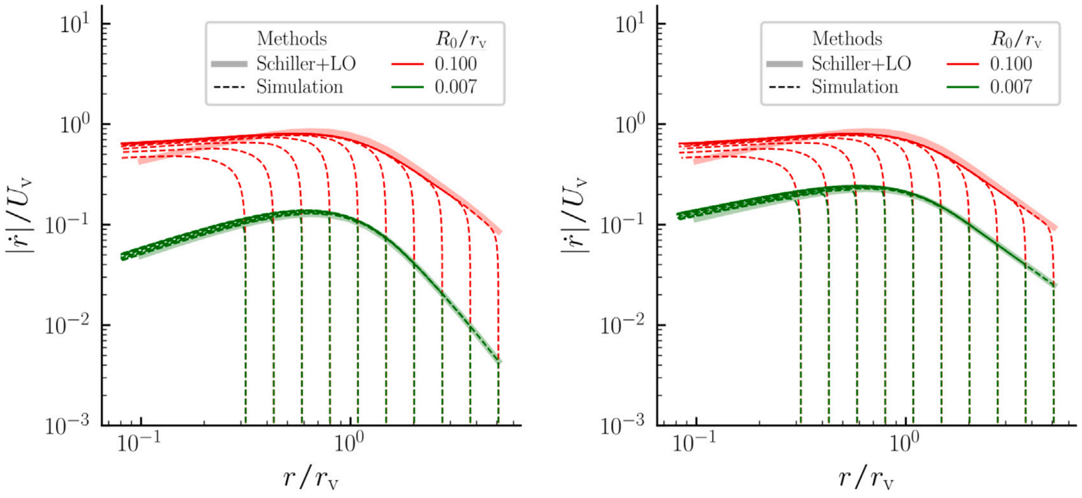

(a) $\Gamma_\infty = 0.29\,\mathrm{m}^2/\mathrm{s}$. (b) $\Gamma_\infty = 29.0\,\mathrm{m}^2/\mathrm{s}$.

Fig. 11. Radial history of normalized radial velocity regarding different circulation strengths. The model predictions (translucent shades; model variation of Schiller drag with the stationary Lamb-Oseen vortex flow field) are compared against the numerical simulation results (the dashed lines). Lines start with different horizontal intercepts stand for bubbles from different release positions, while the red and green colors represent large and small bubbles, respectively.

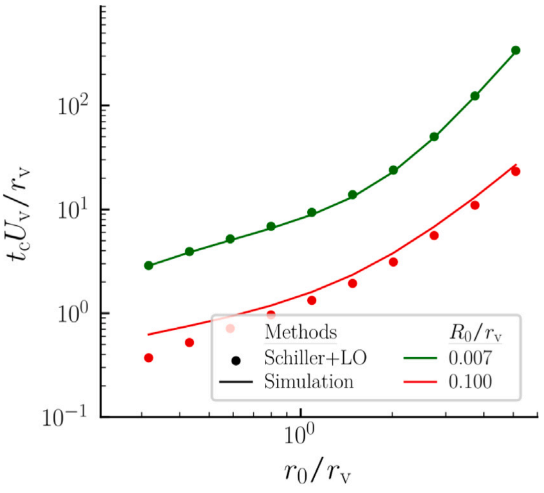

Fig. 12. Normalized capture time as a function of the release position (r_0) via the analytical and numerical approaches. Only the model of Schiller drag formulation with stationary Lamb-Oseen flow field (“Schiller+LO”) is presented. The green and red lines represent small and large bubbles, respectively.

Table 2
Comparison of dimensionless capture time prediction from experiment and model methods. The experiment parameters are $r_0^* = 1.0$, $r_{cap}^* = 0.1$, $\mathrm{Re}_v = 3.3 \times 10^4$.

R_0^*	t_c^* (Exp.)	t_c^* (Model)	Error
0.10	1.25	1.21	3.56%
0.17	0.90	0.94	4.30%

and experimental results (Table 2) demonstrates remarkable accuracy, indicating that the assumptions of radial kinematic dominance and force balance in the azimuthal direction are valid.

In summary, factors that lead to shorter capture times include larger bubble size, closer initial release position, and higher pressure gradient force. The model has limitations in cases where the acceleration is too pronounced to neglect, such as for large bubbles, and when the initial

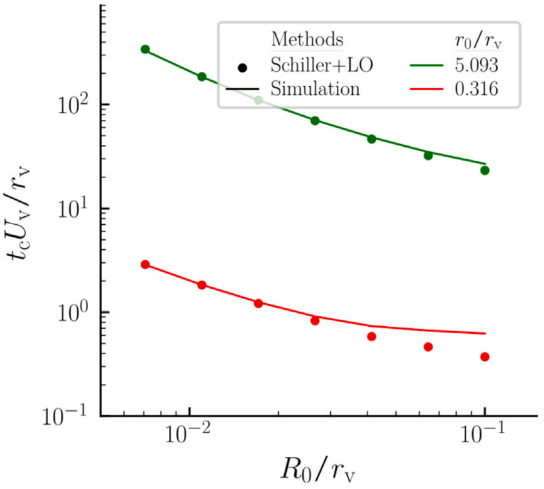

Fig. 13. Normalized capture time as a function of the bubble size (R_0) via the analytical and numerical approaches. Only the model of Schiller drag formulation with stationary Lamb-Oseen flow field (“Schiller+LO”) is presented. The green and red lines represent far- and near-released bubbles, respectively.

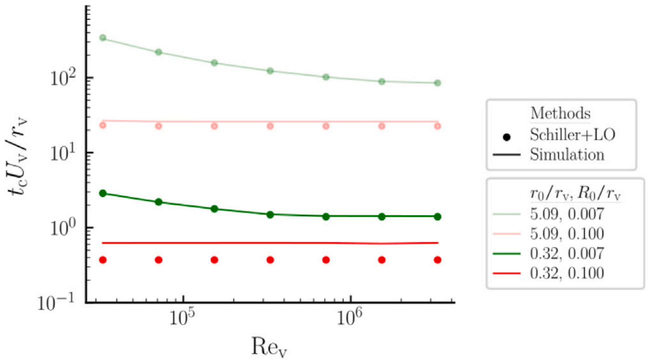

Fig. 14. Normalized capture time as a function of the vortex Reynolds number ($\mathrm{Re}_v = U_v r_v/\nu \sim \Gamma_\infty/\nu$) via the analytical and numerical approaches. Only the model of Schiller drag formulation with stationary Lamb-Oseen flow field (“Schiller+LO”) is presented. The translucent and the opaque lines stand for the far- and near-released bubbles, while the green and red lines represent the small and large bubbles.

acceleration stage contributes significantly to the total traveling time, as may occur for small time scales. In spite of that, the model still provides sufficient accuracy and insight into the capture phenomenon.

7. Conclusion

In this study, the forces acting on bubbles and the capture phenomenon in a stationary Lamb-Oseen vortex flow have been investigated using Lagrangian bubble tracking. The roles of the force components were examined in detail and it was found that the pressure gradient and added mass forces attract and trap the bubble into the vortex core in the radial direction, while the drag and centrifugal forces try to counter and balance out this effect. In addition, the lift force was found to have a significant effect in the azimuthal direction, balancing the Coriolis force and preventing underdamped behavior as the bubbles move toward the vortex center. Without the lift force, bubbles exhibit erratic behavior.

Considering the observed balance of forces, a capture time estimation methodology has been developed. Three factors that have a deterministic effect on the capture time were identified: the normalized initial bubble radius, the normalized initial release location, and the vortex Reynolds number. The numerical results showed that larger bubbles and those released closer to the vortex center are captured more quickly, and that a higher vortex Reynolds number leads to a shorter capture time. Furthermore, the developed model was proven more accurate than what had been presented in previous published studies since it incorporates a more complete description of the relevant physics.

The proposed force balance mechanism and capture time model were both found to show good agreement with the numerical simulation and experimental results. This study provides insight into the conditions that lead to the tip vortex cavitation inception and can inform future research in this area. A potential application of the developed capture time model is to predict the tip vortex cavitation hotspot by inferring the downstream length from the capture time. On the other hand, the force analysis could assist to explain the phenomena observed in numerical simulations or experiments. Future work should address the limitations of the current numerical simulation, focusing mainly on replacing the simplified vortex model with a more realistic representation of a tip vortex flow. A broader range of the chosen initial conditions more closely corresponding to cavitation tunnel conditions should also be investigated.

CRediT authorship contribution statement

Tzu-Yao Huang: Writing – review & editing, Writing – original draft, Visualization, Validation, Software, Methodology, Formal analysis, Data curation, Conceptualization. **Artur K. Lidtke:** Writing – review & editing, Visualization, Validation, Supervision, Software, Methodology, Formal analysis, Data curation, Conceptualization. **Rens Stigter:** Writing – review & editing, Validation, Supervision, Methodology, Formal analysis, Conceptualization. **Martijn X. van Rijsbergen:** Visualization, Supervision, Methodology, Formal analysis, Conceptualization. **Tom J.C. van Terwisga:** Writing – review & editing, Visualization, Supervision, Resources, Project administration, Methodology, Formal analysis, Conceptualization.

Declaration of competing interest

The authors declare that they have no known competing financial interests or personal relationships that could have appeared to influence the work reported in this paper.

Data availability

Data will be made available on request.

Declaration of Generative AI and AI-assisted technologies in the writing process

During the preparation of this work the authors used ChatGPT in order to improve the readability. After using this tool/service, the authors reviewed and edited the content as needed and take full responsibility for the content of the publication.

Appendix A. Planar mechanics in polar coordinates

A minimal description of the polar coordinate as a preliminary is addressed. For further information, readers are referred to the textbooks in dynamics; see Hibbeler (2016) for example.

Two position-dependent unit vectors characterize the particle motion in the description of polar coordinates: an outward-pointing radial direction and a counter-clockwise azimuthal direction. The position vector, $\mathbf{r}$, is defined in

$$\mathbf{r} = r\hat{\mathbf{e}}_r, \tag{25}$$

where $\hat{\mathbf{e}}_r = \cos\theta\hat{\mathbf{i}} + \sin\theta\hat{\mathbf{j}}$ in the Cartesian coordinate. The velocity vector reads

$$\mathbf{v} = \frac{\mathrm{d}}{\mathrm{d}t}\mathbf{r} = \dot{r}\hat{\mathbf{e}}_r + r\dot{\hat{\mathbf{e}}}_r = \dot{r}\hat{\mathbf{e}}_r + r\dot{\theta}\hat{\mathbf{e}}_\theta, \tag{26}$$

where, from their geometrical relationship,

$$\frac{\mathrm{d}}{\mathrm{d}t}\hat{\mathbf{e}}_r = \quad \dot{\theta}\hat{\mathbf{e}}_\theta, \tag{27}$$

$$\frac{\mathrm{d}}{\mathrm{d}t}\hat{\mathbf{e}}_\theta = -\dot{\theta}\hat{\mathbf{e}}_r. \tag{28}$$

Differentiating the velocity formulation yields the acceleration

$$\mathbf{a} = \frac{\mathrm{d}^2}{\mathrm{d}t^2}\mathbf{r} = \left(\ddot{r} - r\dot{\theta}^2\right)\hat{\mathbf{e}}_r + \left(r\ddot{\theta} + 2\dot{r}\dot{\theta}\right)\hat{\mathbf{e}}_\theta. \tag{29}$$

Wherein it contains not only the standard second derivatives of the coordinate axes but also the fictitious term, or the so-called inertial accelerations: $r\dot{\theta}^2$ and $-2\dot{r}\dot{\theta}$, representing the centrifugal and Coriolis accelerations, respectively. One could regard the Coriolis force as the effect of the conservation of the angular momentum: if the bubble moves toward the center, the term will accelerate $\dot{\theta}$. The acceleration without the inertial terms is called the "apparent acceleration", while the total is named "absolute acceleration". The terms should be distinguished carefully in the acceleration analysis.

Appendix B. Simplified bubble motion equation

The development of the capture time model requires a simplification form of the bubble motion equation. Still, the equation applied for the Lagrangian bubble tracking is still in the original form, *i.e.*, the simplified equation is not implemented. In the current case, the bubble mass is significantly smaller than the added mass, and the added mass coefficient is one-half because of the assumed spherical bubble. Eq. (6) could be then simplified into a form of acceleration components via dividing the equation with the added mass ($C_{\mathrm{AM}}\rho V_{\mathrm{B}}$):

$$\frac{\mathrm{d}\mathbf{U}_{\mathrm{B}}}{\mathrm{d}t} = -\frac{2\nabla P}{\rho} - \frac{\nabla P}{\rho} + \frac{3}{4}\frac{C_D}{R}\left|\mathbf{U} - \mathbf{U}_{\mathrm{B}}\right|(\mathbf{U}-\mathbf{U}_{\mathrm{B}}) + (\mathbf{U}-\mathbf{U}_{\mathrm{B}})\times\boldsymbol{\omega} + \frac{3\dot{R}}{R}(\mathbf{U}-\mathbf{U}_{\mathrm{B}}). \tag{30}$$

The right-hand side of the equation includes pressure gradient acceleration, the flow component of added mass acceleration, drag acceleration, lift acceleration, and Kelvin impulse acceleration components, respectively.

References

Abdel-Maksoud, M., Hänel, D., Lantermann, U., 2010. Modeling and computation of cavitation in vortical flow. Int. J. Heat Fluid Flow 31 (6), 1065–1074. http://dx.doi.org/10.1016/j.ijheatfluidflow.2010.05.010.

Afolabi, E., Lee, J., 2014. An Eulerian–Eulerian CFD simulation of air-water flow in a pipe separator. J. Comput. Multiph. Flows 6 (2), 133–149. http://dx.doi.org/10.1260/1757-482X.6.2.133.

Anderson, E.A., Lawton, T.A., 2003. Correlation between vortex strength and axial velocity in a trailing vortex. J. Aircr. 40 (4), 699–704. http://dx.doi.org/10.2514/2.3148.

Arndt, R.E.A., Arakeri, V.H., Higuchi, H., 1991. Some observations of tip-vortex cavitation. J. Fluid Mech. 229, 269–289. http://dx.doi.org/10.1017/S0022112091003026.

Auton, T.R., 1987. The lift force on a spherical body in a rotational flow. J. Fluid Mech. 183, 199–218. http://dx.doi.org/10.1017/S002211208700260X.

Bosschers, J., 2018. Propeller Tip-Vortex Cavitation and its Broadband Noise (Ph.D. thesis). University of Twente, http://dx.doi.org/10.3990/1.9789492679529.

Cheng, H., Long, X., Ji, B., Peng, X., Farhat, M., 2021. A new Euler–Lagrangian cavitation model for tip-vortex cavitation with the effect of non-condensable gas. Int. J. Multiph. Flow 134, 103441. http://dx.doi.org/10.1016/j.ijmultiphaseflow.2020.103441.

Elghobashi, S., 1994. On predicting particle-laden turbulent flows. Appl. Sci. Res. 52 (4), 309–329. http://dx.doi.org/10.1007/BF00936835.

Erbe, C., Marley, S.A., Schoeman, R.P., Smith, J.N., Trigg, L.E., Embling, C.B., 2019. The effects of ship noise on marine mammals – A review. Front. Mar. Sci. 6, 606. http://dx.doi.org/10.3389/fmars.2019.00606.

Finn, J., Shams, E., Apte, S.V., 2011. Modeling and simulation of multiple bubble entrainment and interactions with two dimensional vortical flows. Phys. Fluids 23 (2), 023301. http://dx.doi.org/10.1063/1.3541813.

Hibbeler, R.C., 2016. Engineering Mechanics: Dynamics, fourteenth ed. Pearson.

Hirt, C., Nichols, B., 1981. Volume of fluid (VOF) method for the dynamics of free boundaries. J. Comput. Phys. 39 (1), 201–225. http://dx.doi.org/10.1016/0021-9991(81)90145-5.

Hsiao, C.-T., Chahine, G.L., Liu, H.-L., 2000. Scaling Effect on Bubble Dynamics in a Tip Vortex Flow: Prediction of Cavitation Inception and Noise. Report 98007–1, Dynaflow, Inc..

Hsiao, C.-T., Chahine, G.L., Liu, H.-L., 2003. Scaling Effect on Prediction of Cavitation Inception in a Line Vortex Flow. J. Fluids Eng. 125 (1), 53–60. http://dx.doi.org/10.1115/1.1521956.

Hsiao, C.-T., Pauley, L.L., 1999. Study of tip vortex cavitation inception using Navier–Stokes computation and bubble dynamics model. J. Fluids Eng. 121 (1), 198–204. http://dx.doi.org/10.1115/1.2822002.

Ji, B., Wang, Z., Cheng, H., Bensow, R.E., 2024. Cavitation research with computational fluid dynamics: From Euler–Euler to Euler–Lagrange approach. J. Hydrodyn. 36 (1), 1–23. http://dx.doi.org/10.1007/s42241-024-0001-2.

Johnson, Jr., V.E., Hsieh, T., 1966. The influence of the trajectories of gas nuclei on cavitation inception. In: Proceedings of the 6th Symposium Naval Hydrodynamics. SNH, pp. 163–179.

Keller, J.B., Miksis, M., 1980. Bubble oscillations of large amplitude. J. Acoust. Soc. Am. 68 (2), 628–633. http://dx.doi.org/10.1121/1.384720.

Kelly, R., Goldstein, D.B., Suryanarayanan, S., Botto Tornielli, M., Handler, R.A., 2021. The nature of bubble entrapment in a Lamb–Oseen vortex. Phys. Fluids 33 (6), 061702. http://dx.doi.org/10.1063/5.0053658.

Ku, G., Cheong, C., Seol, H., 2020. Numerical investigation of tip-vortex cavitation noise of an elliptic wing using coupled Eulerian–Lagrangian approaches. Appl. Sci. 10 (17), http://dx.doi.org/10.3390/app10175897.

Latorre, R., 1982. TVC noise envelope – An approach to tip vortex cavitation noise scaling. J. Ship Res. 26 (01), 65–75. http://dx.doi.org/10.5957/jsr.1982.26.1.65.

Mathai, V., Lohse, D., Sun, C., 2020. Bubbly and buoyant particle-laden turbulent flows. Annu. Rev. Condens. Matter Phys. 11 (1), 529–559. http://dx.doi.org/10.1146/annurev-conmatphys-031119-050637.

Mazzitelli, I.M., Lohse, D., Toschi, F., 2003. On the relevance of the lift force in bubbly turbulence. J. Fluid Mech. 488, 283–313. http://dx.doi.org/10.1017/S0022112003004877.

Moore, D.W., Saffman, P.G., Stewartson, K., 1973. Axial flow in laminar trailing vortices. Proc. R. Soc. A 333 (1595), 491–508. http://dx.doi.org/10.1098/rspa.1973.0075.

Morrison, Jr., F.A., Stewart, M.B., 1976. Small bubble motion in an accelerating liquid. J. Appl. Mech. 43 (3), 399–403. http://dx.doi.org/10.1115/1.3423879.

Oweis, G.F., van der Hout, I.E., Iyer, C., Tryggvason, G., Ceccio, S.L., 2005. Capture and inception of bubbles near line vortices. Phys. Fluids 17 (2), 022105. http://dx.doi.org/10.1063/1.1834916.

Peters, A., el Moctar, O., 2020. Numerical assessment of cavitation-induced erosion using a multi-scale Euler–Lagrange method. J. Fluid Mech. 894, A19. http://dx.doi.org/10.1017/jfm.2020.273.

Phillips, W.R.C., 1981. The turbulent trailing vortex during roll-up. J. Fluid Mech. 105, 451–467. http://dx.doi.org/10.1017/S0022112081003285.

Prosperetti, A., Lezzi, A., 1986. Bubble dynamics in a compressible liquid. Part 1. First-order theory. J. Fluid Mech. 168, 457–478. http://dx.doi.org/10.1017/S0022112086000460.

Rule, J.A., Bliss, D.B., 1998. Prediction of viscous trailing vortex structure from basic loading parameters. AIAA J. 36 (2), 208–218. http://dx.doi.org/10.2514/2.7503.

Saffman, P.G., 1965. The lift on a small sphere in a slow shear flow. J. Fluid Mech. 22 (2), 385–400. http://dx.doi.org/10.1017/S0022112065000824.

Schiller, L., Neumann, A., 1933. Uber die grundlegenden berechnungen bei der schwerkraftaufbereitung. Z. Ver. Deutsch. Ingen. 77, 318–321.

Sokolichin, A., Eigenberger, G., Lapin, A., Lübert, A., 1997. Dynamic numerical simulation of gas-liquid two-phase flows Euler/Euler versus Euler/Lagrange. Chem. Eng. Sci. 52 (4), 611–626. http://dx.doi.org/10.1016/S0009-2509(96)00425-3.

Sridhar, G., Katz, J., 1995. Drag and lift forces on microscopic bubbles entrained by a vortex. Phys. Fluids 7 (2), 389–399. http://dx.doi.org/10.1063/1.868637.

Uberoi, M.S., Shivamoggi, B.K., Chen, S.-S., 1979. Axial flow in trailing line vortices. Phys. Fluids 22 (2), 214–217. http://dx.doi.org/10.1063/1.862570.

Vallier, A., 2013. Simulations of Cavitation - from the Large Vapour Structures to the Small Bubble Dynamics (Ph.D. thesis). Lund University.

van Rijsbergen, M., Lidtke, A.K., 2020. Sheet cavitation inception mechanisms on a NACA 0015 hydrofoil. In: Proceedings of 33rd Symposium on Naval Hydrodynamics. SNH, pp. 1–23.

van Terwisga, T.J.C., Fitzsimmons, P., Li, Z., Foeth, E.-J., 2009. Cavitation erosion – A review of physical mechanisms and erosion risk models. In: Proceedings of the 7th International Symposium on Cavitation. CAV2009, pp. 1–13.

van Wijngaarden, E., Bosschers, J., Kuiper, G., 2005. Aspects of the cavitating propeller tip vortex as a source of inboard noise and vibration. In: Proceedings of the ASME 2005 Fluids Engineering Division Summer Meeting. In: Fluids Engineering Division Summer Meeting, Vol. 2: Fora, pp. 539–544.

Wang, X., Bai, X., Cheng, H., Ji, B., Peng, X., 2023. Numerical investigation of how gap size influences tip leakage vortex cavitation inception using a Eulerian–Lagrangian method. Phys. Fluids 35 (1), 012113. http://dx.doi.org/10.1063/5.0131813.

Zhang, L., Chen, L., Shao, X., 2016. The migration and growth of nuclei in an ideal vortex flow. Phys. Fluids 28 (12), 123305. http://dx.doi.org/10.1063/1.4972275.